



Molecular dynamics simulation of femtosecond ablation and spallation with different interatomic potentials

V.V. Zhakhovskii^{a,*}, N.A. Inogamov^c, Yu.V. Petrov^c, S.I. Ashitkov^b, K. Nishihara^a

^a Institute of Laser Engineering, Yamada-oka 2-6, Suita, Osaka 565-0871, Japan

^b Joint Institute of High Temperature RAS, 13/19 Izhorskaya Street, Moscow 125412, Russia

^c L.D.Landau Institute for Theoretical Physics RAS, Chernogolovka 142432, Russia

ARTICLE INFO

Article history:

Available online 21 April 2009

PACS:

02.70.Ns

79.20.Ds

52.38.Mf

Keywords:

Molecular dynamics

EAM potential

Femtosecond laser ablation

ABSTRACT

Fast heating of target material by femtosecond laser pulse (fsLP) with duration $\tau_L \sim 40\text{--}100$ fs results in the formation of thermomechanically stressed state. Its unloading may cause frontal cavitation of subsurface layer at a depth of 50 nm for Al and 100 nm for Au. The compression wave propagating deep into material hits the rear-side of the target with the formation of rarefaction wave. The last may produce cracks and rear-side spallation. Results of MD simulations of ablation and spallation of Al and Au metals under action fsLP are presented. It is shown that the used EAM potentials (Mishin et al. and our new one) predict the different ablation and spallation thresholds on absorbed fluence in Al: ablation $F_a = 60\{65\}$ mJ/cm² and spallation $F_s = 120\{190\}$ mJ/cm², where numbers in brackets { } show the corresponding values for Mishin potential. The strain rate in spallation zone was 4.3×10^9 1/s at spallation threshold. Simulated spall strength of Al is 7.4{8.7} GPa, that is noticeably less than 10.3{14} GPa obtained from acoustic approximation with the use of velocity pullback on velocity profile of free rear surface. The ablation threshold $F_a \approx 120$ mJ/cm² and crater depth of 110 nm are obtained in MD simulations of gold with the new EAM potential. They agree well with experiment.

© 2009 Elsevier B.V. All rights reserved.

1. Introduction

The ultrashort laser-matter interaction with pulse duration less than 1 ps and moderate fluence ~ 1 J/cm² is important for fundamental physics of fast processes, warm dense matter physics as well as for a wide range of industrial applications [1–3]. The depth of photon (or multiphoton for intensity $> 10^{12}$ W/cm²) absorption can be a few nanometers in metals. As a result the fsLP may induce nanoscale phenomena in absorbing material without significant warming up and damage of the material surrounding the focal spot. The time and length scales of the processes involved provide an exceptional opportunity to apply MD simulation to study fundamental atomic-scale mechanisms of materials response to fsLP at the level of detail that is difficult or impossible to obtain from experiment.

There are two problems in MD approach. Firstly, it should be combined with another model capable of evaluating the electron and ion temperature in material as functions of position and time during several picoseconds from starting of

absorption of fsLP. The works [2] propose such model. Secondly, for the problem of laser-matter interaction the appropriate interaction potential is a prime necessity to describe material properties realistically and adequately in wide range of pressure, temperature and density. For instance the much used embedded atom model (EAM) potentials of Mishin et al. [4] and Ercolessi–Adams [5] are well optimized for aluminum nearby standard conditions, but not for highly compressed and rarefied states peculiar to material under action of fsLP.

2. New analytical EAM potential

To simulate the behavior of aluminum crystal under action of strong compression and rarefaction waves we develop a new analytical EAM potential based on cold pressure curves evaluated from the density functional theory (DFT).

The common form of EAM potential is given by

$$E_{tot} = \sum_i F(n_i) + \sum_{i<j} V(r_{ij}), \quad n_i = \sum_{k \neq i} n(r_{ik}), \quad (1)$$

where $V(r_{ij})$ is a pair potential, $F(n_i)$ is an embedding energy of i -atom, and $n(r_{ik})$ is a density function. The both mentioned above EAM potentials [4,5] use a cubic spline representation of these

* Corresponding author. Tel.: +81 6 6879 8744.

E-mail address: basil@ile.osaka-u.ac.jp (V.V. Zhakhovskii).

functions. Here we introduce an analytical EAM potential for aluminum as follows

$$x = a_1 r^2, \quad x_c = a_1 r_c^2,$$

$$V(r) = \left(\frac{1}{x} - a_2\right)(x - x_c)^{10}((x - x_c)^6 + a_3 x^6) \quad (2)$$

$$F(n) = \frac{b_1 n(b_2 + (b_3 + n)^2)}{1 + b_4 n} \quad (3)$$

$$n(r) = \frac{c_1(r^2 - r_c^2)^2}{1 + (c_2 r^2)^3} \quad (4)$$

where $r_c = 0.6875$ nm is chosen as a cutoff radius.

The fitting parameters a_N, b_N, c_N were found by minimizing the sum of deviations from components of cold pressure tensor evaluated by using the ABINIT code [6] and the experimental Al properties at $T = 0$ K taken from [5]. The Al lattice constant is 0.4032 nm, cohesive energy -324.19 kJ/mol, and bulk modulus 80.9 GPa. These experimental points have the largest weights in the fitting procedure.

The calculations of cold pressure curves are based on the DFT with local density approximation and by using of the Troullier–Martins pseudopotentials for Al, code is available on [6]. The plane-wave cutoff energy was 871 eV. The EAM potential has two well-known invariant transformations, thus two additional conditions are imposed on fitting parameters. First is $n_{eq} = 1$ for an equilibrium crystal at $P = T = 0$, and second is $F'(n_{eq}) = 0$. These conditions are satisfied exactly by parameters presented in Table 1, where nm as unit of length and kJ/mol as unit of energy are used. The powers in Eqs. (2)–(4) were also adjusted to fit data better. The new potential with fitting parameters from Table 1 reproduces the Al properties with good accuracy. It gives 0.4032 nm for Al lattice constant, -324.258 kJ/mol for cohesive energy, 81.57 GPa for Al bulk modulus at $P = T = 0$, and 940 K for melting point.

The cold pressure components $P(V/V_0, T = 0)$ evaluated by ABINIT as functions of relative uniform and uniaxial $\langle 100 \rangle$ compression-stretching are shown by symbols in Fig. 1. The calculated cold pressure curves represented by lines in Fig. 1 indicate the significant difference in the largest stress σ^* at which Al ruptures. Mishin potential overestimates σ^* about 4 GPa for the uniaxial $\langle 100 \rangle$ stretching of ideal Al crystal. As we show below it results in higher spall strength than one predicted by MD simulation with the new Al EAM potential.

For gold the similar form of EAM potential as in Eqs. (2)–(4) and the same minimization procedure were used to find the fitting parameters a_N, b_N, c_N and powers of new Au EAM potential, see

Table 1
EAM potentials Eqs. (2)–(5) for aluminum and gold.

N	a_N in $V(r)$ for Al	a_N in $V(r)$ for Au
1	2.9275228176598036	2.7471581015136728
2	5.1028014804162156	5.3593750000000000
3	111.37742236893590	3.2500000000000000
N	b_N in $F(n)$ for Al	b_N in $F(n)$ for Au
1	8.1106000931637006	8.2311259601633768
2	-334.57493744623503	-382.38931538388255
3	14.868297626731845	16.250071667347235
4	1.6080953931773090	1.4586663896542300
N	c_N in $n(r)$ for Al	c_N in $n(r)$ for Au
1	0.58002942432410864	3.0697898737897571
2	8.2981185422063639	20.750105835621902

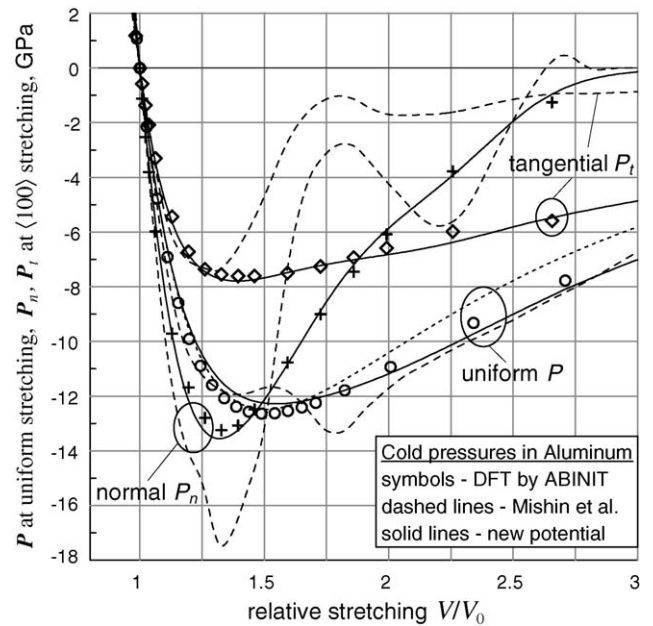


Fig. 1. The cold uniform pressure P , normal P_n and tangential P_t components of pressure tensor obtained by new Al EAM potential, Mishin et al. [4], DFT ABINIT [6], and from the EOS by Rose et al. [7](dotted line).

Table 1. The pair potential function Eq. (2) is replaced by Eq. (5) optimized for Au:

$$V(r) = \left(\frac{1}{x} - a_2\right)(x - x_c)^{10}((x - x_c)^{18} + a_3) \quad (5)$$

The new potential gives 0.4065 nm for Au lattice constant, -367.609 kJ/mol for cohesive energy, 179.4 GPa as a bulk modulus at $P = T = 0$, and ~ 1330 K for melting point of Au. Fig. 2 shows the cold pressure components evaluated by ABINIT and new Au EAM potential. The new EAM potentials provide also good fits of pressure curves evaluated by ABINIT and Rose EOS [7] for large stretching as indicated in Figs. 1 and 2 as well as for large compression ratio V/V_0 up to 0.5 and pressure ~ 1000 GPa.

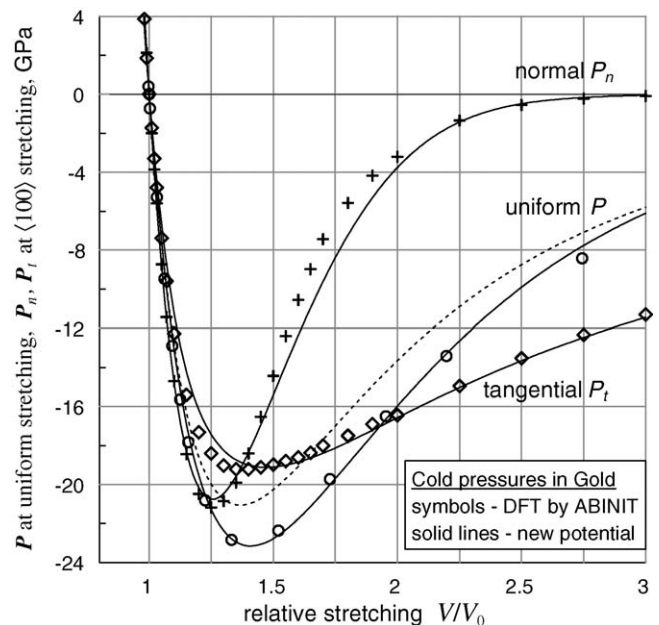


Fig. 2. The cold pressure $P(V/V_0, T = 0)$ components obtained by new Au EAM potential, DFT ABINIT, and from Rose's EOS (dotted line).

It should be particularly emphasized that the proposed EAM potentials Eqs. (2)–(5) was optimized only for cold pressure components in uniform and uniaxial (1 0 0) compression-stretching. We checked the accuracy of these potentials by comparison with ABINIT cold pressures for stretching along (1 1 0) directions, and found that the agreement between them is not so good as shown in Figs. 1 and 2 but still remains much better than for Mishin et al. potential. Another weakness comes from the incorrect exponential asymptotic decay of LDA exchange–correlation potential with distance, instead of correct $\sim 1/r$ behavior. The possible solution is the using of Hartree–Fock methods to obtain more precise cold pressures for high stretching $V/V_0 \gtrsim 2$. We guess that the pressure minima in Figs. 1 and 2 are calculated properly for “low” stretching $V/V_0 < 1.5$, that is essential for correct simulation of cavitation and spallation.

3. Ablation threshold vs cohesion energy

There are two significantly different potentials used extensively in MD simulation of materials: pairwise potentials like Lennard–Jones and Morse and manybody potentials like EAM used for simulation of metals. These potentials correspond to narrow and wide potential wells, respectively. The influence of well shape on ablation dynamics attracts particular interest.

Atoms in crystal lattice with narrow potential wells like smoothed LJ (sLJ) potential [8] rigidly interact with each other. It results in higher activation energy of self-diffusion. By contrast, atom diffusion in crystal with wide potential wells is much easier, and it becomes possible for much lower T/E_{coh} .

Fig. 3 shows potential barriers $A(x)$ along relocation path of an atom from its initial site to the final unoccupied vacancy site as a function of the relative position for sLJ and new Al EAM potential. Potential barriers are normalized by cohesion energy E_{coh} . sLJ parameters fitted on Al density and cohesion energy are $\varepsilon = 41.763$ kJ/mol and $\sigma = 0.26046$ nm. Our new Al EAM potential gives vacancy formation energy in unrelaxed crystal $E_{v, fu} = 72.92$ kJ/mol and $E_{v, f} = 72.01$ kJ/mol in relaxed crystal. Vacancy migration energies $E = A_{max}(x = 1/2)$ in unrelaxed and relaxed crystals are as follows: $E = 90.39$ and $E = 56.01$ kJ/mol. It gives the activation energy of diffusion $E_D = E_{v, f} + E = 128.02$ kJ/mol, which is in a good agreement with experimental value of 128.3 kJ/mol [9]. Atoms in sLJ fcc crystal have the highest energy barrier to change their location in a lattice. Morse potential holds

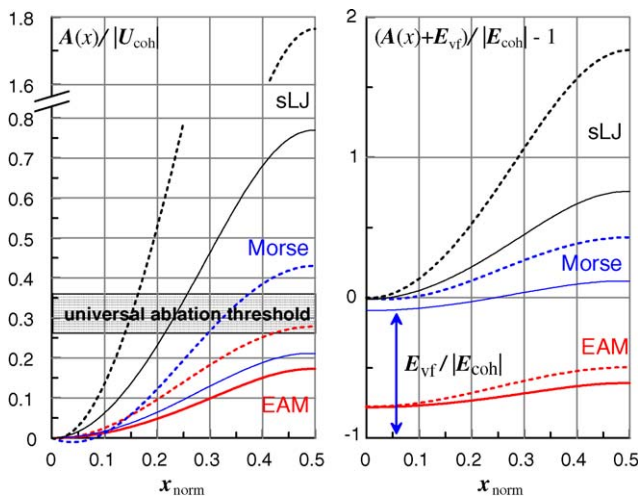


Fig. 3. Potential barrier $A(x)$ for vacancy migration in Al crystals simulated by sLJ, Morse, and new EAM potential. Dotted lines correspond to unrelaxed fcc crystal, solid lines—crystal relaxed at each point of straight migration path of an atom to vacancy site.

an intermediate position, and Al EAM has the lowest barrier as indicated by Fig. 3.

Therefore it is not surprising that there is large difference between thermodynamic phase diagrams for cases of narrow and wide potentials. The ratios of parameters in the triple point to cohesion energy E_{tp}/E_{coh} or to critical temperature T_{tp}/T_c are lower for wider potentials. Crystal with wide potential like EAM melts easily as against narrow sLJ.

On the other hand evaporation depends mainly on potential well depth rather than its shape. Clausius–Clapeyron relation gives formula of vapor pressure $\ln P \approx \text{Const} - E_{coh}/T$, which essentially depends on sublimation energy or E_{coh} . Thermomechanical ablation is believed to be another example of process that is depends mostly on cohesion energy. Indeed, to stretch and rupture material is necessary to overcome its resistance. The work of stretching $E_{coh} = -\int_{V_0}^{\infty} P(V) dV$ from specific volume $V_0(P = T = 0)$ along cold pressure curve $P(V/V_0, T = 0)$ gives the cohesion energy.

Fig. 4 shows cold pressure curves for cases of wide (new Al EAM potential) and narrow sLJ potentials. It must be emphasized that the cohesion energies are equal for both potentials despite their different shapes of $P(V)$. The energy $S \sim 0.2E_{coh}$ required for stretching of material until spinodal point at $T = 0$ (minimum of the cold pressure in Fig. 4) are very closed to each other for both potentials.

The actual thermomechanical fragmentation takes place with $T > 0$, and material fragments before its stretching up to the spinodal point. In addition, after the initial elastic part of expansion and before fragmentation, the plastic effects may take place [10,11], these also change dependence $P(V, T)$. Near ablation threshold some addition work is required for formation of bubble surfaces [12]. All these factors contribute to value of E_a required for fragmentation. Here E_a is an addition to the internal energy of atom, which is necessary to achieve ablation threshold during fast heating of initially cold material.

The energy deposited by fsLP in target material shares between potential and kinetic energy of atoms in equal parts roughly. Hence, to reach the spinodal line the deposited energy per an atom should be twice more $S(T_s) \sim 2S(0) \approx 0.4E_{coh}$. It was found [13] that the normalized thresholds $E_a/E_{coh} \sim 0.27–0.37$ weakly depends on shape of the potential well. Such universality indicates that the thermomechanical spallation is defined mainly by the depth of potential well (or cohesion energy) as illustrated in Fig. 3.

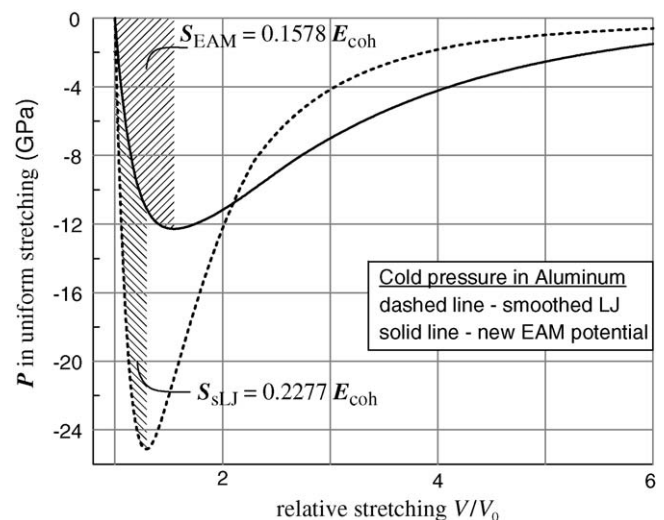


Fig. 4. The cold pressures $P(V/V_0)$ obtained by new EAM potential and smoothed LJ in uniform expansion of ideal Al crystal at $P = T = 0$.

4. Simulation results

We use the *MPD*³ algorithm [14] for large-scale parallel MD simulation of Al foil. At $t = 0$ the motionless target is an ideal Al crystal having the face-centered cubic lattice at zero pressure and room temperature. The crystal has a rectangular form with dimensions $l_x \times l_y \times l_z$ and periodical conditions imposed along the y, z -directions. The crystal direction [1 1 0] is aligned with x -axis, and the longest $l_x = 689$ nm. The maximal number of atoms in MD box with dimensions $l_x \times l_y \times l_z = 537.38$ nm \times 48.78 nm \times 48.87 nm was 76,296,000. The initial temperature $T_0(x)$ is formed by heating up Al atoms during $\tau = 1-2$ ps by Langevin thermostat with forces $\Xi(x_i) = \xi(x_i) - \beta m_i v_i$, where $\xi(x_i)$ is a position-dependent Gaussian random force applied to i -atom with mass m_i and velocity v_i , and β is a friction coefficient. To obtain a prescribed temperature $T(x)$, the variance of distribution $\xi(x_i)$ should satisfy the condition $\sigma_i^2 = 2\beta m_i k_B T(x_i)/h$. The integration time step was $h = 2$ fs for $T_0 < 4$ kK, and $h = 1$ fs for higher temperatures, and $\beta = 1/200h$ in our MD simulations. Langevin thermostat operated for first 1000 simulation steps and then shut down.

'Supersonic' formation of pressurized region near the vacuum boundary during time shorter than d_T/c_s has two important mechanical effects. First, a matter begins to expand towards vacuum due to movement of rarefaction wave. This wave causes the frontal thermomechanical ablation. Second, the compression wave propagates to the right and results in rear-side spallation at the right vacuum boundary B shown in Fig. 5. The shape of twofold pulse is changed slowly due to the small sound velocity dispersion. The focusing of characteristics results in the breaking of compression wave with creation of the leading shock S_f . The shock S_e on the trailing front of twofold wave appears due to the cavitation rupture of Al melt. Shocks S_e and S_f are the left and right ends of rarefaction wave.

It is found that the difference between EAM potentials has limited effect on pressure wave profiles as shown in Fig. 5. It weakly affects on the cavitation in melted front-side layer. By contrast, the pressures simulated by Mishin and our potential in the region of negative pressure appearing after wave reflection

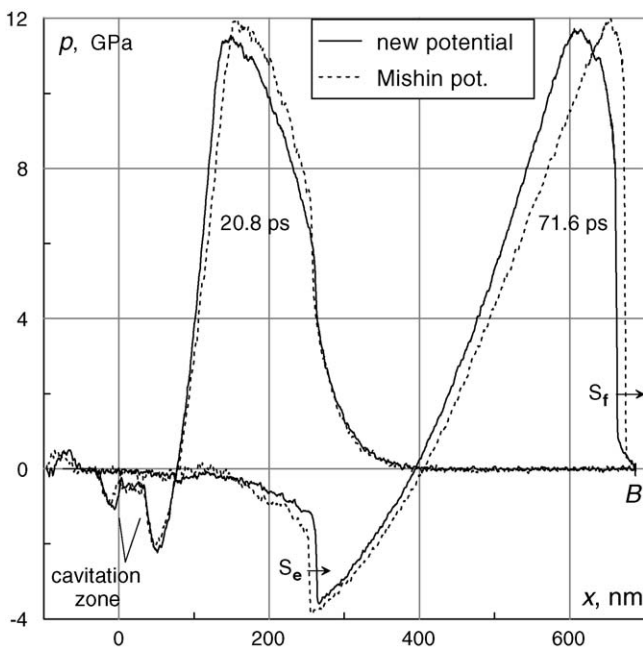


Fig. 5. The quasi-steady twofold wave with two shocks S_e, S_f in Al target.

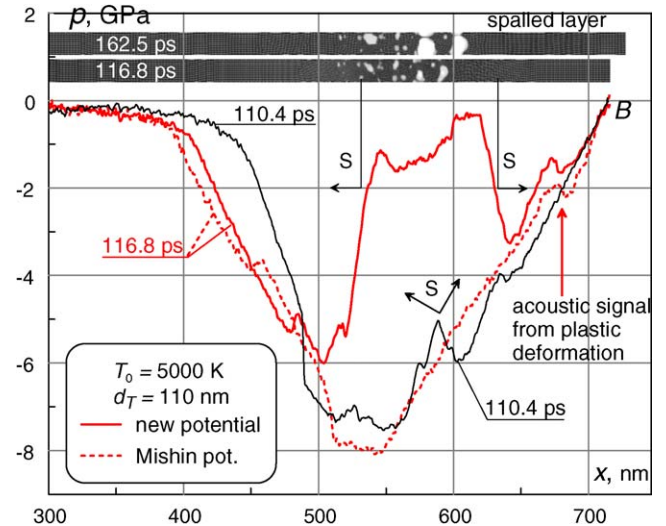


Fig. 6. Pressure profiles for two moments from MD simulation of the rear-side spallation by the new Al EAM (solid lines) and Mishin potentials at $T_0 = 5$ kK. Two maps of density of rear-side part of target on the top.

from the rear-side vacuum boundary substantially differ from one another as indicated by Fig. 6.

Fig. 6 shows the rear-side spallation of Al foil with initial frontal temperature $T_0 = 5$ kK. After reflection the shock denoted S_f in Fig. 5 transforms into the rarefaction wave. Uniaxial stretching causes shear stress to rise up to some critical value about 1.8 GPa with a consequent plastic deformation of Al crystal. This process starts from 102.8 ps and involves a wide zone ~ 80 nm thick. After approximately 6 ps the first fracture (void) appears on the right end of plastic zone. The spallation begins near the maximum of stretching stress $\sigma^* \approx 7.4\{8.7\}$ GPa, where numbers in brackets $\{ \}$ obtained with Mishin potential. The strain rate in spallation zone was 4.3×10^9 1/s in MD simulation with absorbed fluence slightly above spallation threshold $F_s = 120\{190\}$ mJ/cm², which corresponds to the initial temperature $T_s = 3.5\{6\}$ kK on frontal surface of the target. Over the next 6 ps many new voids appear and

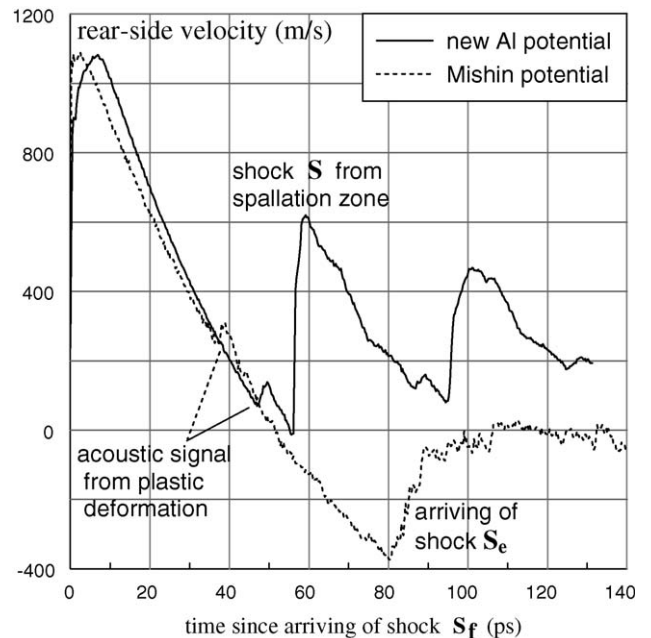


Fig. 7. Velocities of free surface of spalled layer (solid line by new EAM potential) and unbroken Al target (dots by Mishin potential) at $T_0 = 5$ kK.

occupy the zone from right to left. The pressure rapidly goes up to zero forming two shocks S having speed ~ 8 km/s. After ~ 85 ps from nucleation of first crack the spalled layer ~ 100 nm thick eventually detaches from the target.

Velocities of rear-side surface of the spalled layer (simulated by new Al EAM potential) and unbroken target (by Mishin potential) as function of time for initial frontal $T_0 = 5$ kK are shown in Fig. 7. The velocity jump up to 1.1 km/s is induced by arriving shock S_f . Then this velocity decreases until arriving of shock S from spallation zone. The velocity pullback $\Delta u = 1.1$ km/s, defined as a difference between these maximal and minimal velocities, can be used in linear acoustic approximation [16] to obtain the spall strength of material from formula $\sigma^* = \rho_0 c_l \Delta u / 2$, where ρ_0 is an initial density and $c_l = 6.9$ km/s is the sound speed along $\langle 110 \rangle$ directions of ideal Al EAM crystal. It gives the spall strength of 10.3{14} GPa, which is significantly higher than simulated one 7.4{8.7} GPa as a result of decreasing of sound speed with stretching.

5. Conclusion

The temperature thresholds obtained in MD simulations with our new Al EAM potential are $T_a = 2.3\{2.55\}$ kK for ablation and $T_s = 3.5\{6\}$ kK for spallation {numbers in brackets for Mishin potential}. The fluence thresholds are $F_a = 60\{65\}$ mJ/cm² for ablation and $F_s = 120\{190\}$ mJ/cm² for spallation. Spall strength of simulated Al is found to be 7.4{8.7} GPa. The evaluated crater depth is 48 nm for simulations with the number of atoms $N \approx 76 \times 10^6$ and the large yz -cross section 49 nm \times 49 nm of MD box. The threshold temperature T_a and F_a are 2% higher for the MD simulations with smaller yz -cross section 7 nm \times 7 nm. The difference in potentials shifts the ablation threshold by 10% and the spallation threshold by 50%, and the ratio of thresholds F_s/F_a changes from 3 to 2.

The experiments [15] give the ablation threshold for absorbed fluence $F_a = 0.064\text{--}0.07$ J/cm² and the corresponding crater depth 50 nm in Al. The both characteristics are in an excellent agreement with simulated ones. The ablation threshold of gold obtained in MD simulation $F_a \approx 0.12$ J/cm² and crater depth of 110 nm. They agree also well with experiments [17].

The physics of spallation has received much attention [16]. There are a variety of devices such as explosives, ion beams, lasers, which differ in length scales and deformation rates \dot{V}/V . As it was already demonstrated, the pump-probe laser system with frequency-domain interferometry can provide a tool to measure nanoscale displacement of rear-side induced by arriving shock [18]. We propose to send the probe beam to both surfaces of a film (frontal and rear-side) to perform the measurement of frontal and rear-side displacements in single experiment. We hope that the pump-probe laser system can operate as a VISAR system, providing nanoscale displacement measurements. Such experiments will allow to obtain information about the spall strength of material at very high strain rate $\dot{V}/V \sim 10^{10} \text{ s}^{-1}$.

Acknowledgment

The work is supported by the RFBR grant No. 07-02-00764.

References

- [1] A.N. Volkov, L.V. Zhigilei, J. Phys.: Conf. Ser. 59 (2007) 640–645.
- [2] M.B. Agranat, JETP Lett. 85 (6) (2007) 271.
- [3] S.I. Anisimov, JETP 103 (2006) 183–197.
- [4] Y. Mishin, D. Farkas, M.J. Mehl, D.A. Papaconstantopoulos, Phys. Rev. B 59 (1999) 3393–3407.
- [5] X.-Y. Liu, F. Ercolessi, J.B. Adams, Model. Simul. Mater. Sci. Eng. 12 (2004) 665.
- [6] The ABINIT code is a common project of the Universite' Catholique de Louvain, Corning Incorporated, and other contributors (<http://www.abinit.org>).
- [7] J.H. Rose, J.R. Smith, F. Guinea, J. Ferrante, Phys. Rev. B 29 (1984) 2963.
- [8] V.V. Zhakhovskii, S.V. Zybin, K. Nishihara, S.I. Anisimov, Phys. Rev. Lett. 83 (1999) 1175.
- [9] S. Dais, R. Messer, A. Seeger, Mater. Sci. Forum 15–18 (1987) 419.
- [10] S.I. Anisimov, JETP Lett. 77 (2003) 606–610.
- [11] S.I. Anisimov, Appl. Surf. Sci. 253 (2007) 6390–6393.
- [12] V.V. Zhakhovskii, JETP Lett. 87 (2008) 423–427.
- [13] A. Upadhyay, N. Inogamov, B. Rethfeld, H. Urbassek, Phys. Rev. B 78 (2008) 045437.
- [14] V.V. Zhakhovskii, IEEE Proceeding of the 5th International Symposium on Cluster Computing and Grid (CCGrid 2005), vol. 2, 2005, p. 848.
- [15] S.I. Anisimov, Appl. Phys. A 939 (2008) 92.
- [16] G.I. Kanel, S.V. Razorenov, V.E. Fortov, L. Davidson, Y. Horie, Shock-Wave Phenomena and the Properties of Condensed Matter, Springer, 2004.
- [17] N.A. Inogamov, JETP 133 (2008) 1–24.
- [18] R. Evans, Phys. Rev. Lett. 77 (1996) 3359–3362.